

Universal symmetry of optimal control at the microscale

Sarah A. M. Loos,¹ Samuel Monter,² Felix Ginot,² and Clemens Bechinger²

¹*DAMTP, Centre for Mathematical Sciences, University of Cambridge, Cambridge, United Kingdom*

²*Faculty of Physics, University of Konstanz, Konstanz, Germany*

(Dated: November 2, 2023)

Optimal control is an important field in thermodynamics, mathematics and engineering which searches for strategies e.g. to move an object to a target position within a given time with minimal energetic effort [1–4]. Especially for micro- and nanomachines [5–7], for which power supply is often limited, knowledge of optimal control protocols is crucial for their operation under realistic conditions [8]. Here we investigate experimentally and theoretically the optimal protocol for transporting a microscopic colloidal particle with an optical trap in such a way that the required work is minimal. The experiments were conducted in viscous and viscoelastic media, which represent typical environments for synthetic and biological nanomachines. Despite marked differences between the protocols in both fluids, we find that the optimal transport protocol and the corresponding average particle trajectory always obeys time-reversal symmetry. This symmetry, which surprisingly appears here for a class of processes far away from thermal equilibrium, is moreover expected to hold universally for e.g. active, granular and long-range correlated media in their linear regimes. The uncovered symmetry provides a rigorous and versatile criterion for optimal control which greatly facilitates the search of energy-efficient transport strategies in a wide range of systems.

The increasing quest of energy-efficient machines and processes is not limited to macroscopic length scales. Due to ongoing miniaturization, micro- and nanoscopic machines are within reach and there is great need to identify optimal control strategies that enable their efficient operation [6, 7]. This is also motivated by biological engines (molecular motors) which demonstrate that even at high frequencies and in the presence of liquid environments, high efficiencies can be achieved [8, 9]. At first glance, this seems to be in contradiction with conventional heat engines where maximal efficiency is only reached for infinitely slow, i.e., quasi-static motion [10–14]. Recent studies of molecular machines suggest that by regulating their power according to the external resistance, excessive dissipation can be avoided [2, 15].

The energy-efficient operation of nanomachines is a specific example of a finite-time, (near-)optimal driving process. Such processes are not only important for small-scale robotic applications [5–7] but also in various other fields like plant physiology [16], molecular biology [17], as well as classical [4] and quantum information processing [3, 18]. As a generic example of a finite-time optimal process, theoretical studies have considered the highest energy-efficient transport of a micron-sized particle through a viscous environment. Surprisingly, this is achieved by a non-steady forcing with jump discontinuities at the beginning and end [1].

So far, experimental and theoretical studies on optimal driving processes have mainly considered viscous environments that remain in equilibrium in the presence of a driven particle. Typically, however, molecular motors or microrobots operate within more complex surroundings. Common environments are viscoelastic media (e.g., intracellular plasma [19], blood [20], polymeric gels [21, 22], micellar solutions [23], or colloidal suspensions [24, 25]) which do not remain in equilibrium during operation due to their slowly relaxing microstructure. This leads to

pronounced memory effects, i.e. non-Markovian behavior of driven particles in such media, which are absent in purely viscous (memory-free) liquids [26, 27].

Here, we experimentally and theoretically investigate the optimal transport of a Brownian particle driven by optical tweezers which move over a given distance within a given time, such that the average work spend on the particle is minimal. In viscous liquids, our experiments confirm previously predicted driving discontinuities at the beginning and the end of the protocol and a constant driving power in between [1]. For viscoelastic fluids, however, no constant driving regime is found due to the presence of memory effects. Astonishingly, despite the fundamentally different optimal protocols in viscous and viscoelastic fluids, we find that both the mean particle trajectory and the protocol for optimal transport exhibit a time-reversal symmetry. Starting from a generalized Langevin equation, we theoretically prove that this symmetry generally arises irrespective of the specific memory kernel or noise property as long as all forces are linear. Therefore, time-reversal symmetry allows a clear distinction to identify optimal transport in various systems including granular [28] and active [29, 30] media, or fluids with hydrodynamic backflow [31] or anomalous diffusion [32]. Beyond their implications for the optimal operation of micromachines in complex environments, our findings suggest the use of symmetry considerations is a powerful tool to significantly expedite optimization problems, or even to allow finding optimal driving protocols.

EXPERIMENTAL SETUP

Our experiments were performed using spherical silica particles (diameter $\approx 2.7\mu\text{m}$) suspended in a fluid contained in a sample cell with $100\mu\text{m}$ height. In addition to a purely viscous water-glycerol mixture (1:1), we used

a viscoelastic solution composed of cetylpyridinium chloride monohydrate (CPyCl) and sodium salicylate (NaSal) (for details see Methods). At the used concentration of 8 mM a worm-like micellar micro-network is formed [33] whose relaxation time was experimentally determined to $\tau_b \approx 17$ s (see Methods). A laser beam (532 nm) is focused with an objective (NA = 1.45, 100x) into the mid-plane of the sample cell (see Fig. 1a) where it creates a parabolic optical potential

$$V(X, \lambda) = \frac{\kappa}{2}(X - \lambda)^2. \quad (1)$$

Here, κ denotes the trap stiffness, X the particle position and λ the time-dependent trap center location, which is the control parameter. Experimentally, a dynamical variation of λ with time t was realized by translating the sample cell relative to a static optical trap. The positions of the particle and the trap were determined by digital video microscopy with a spatial and temporal resolution of 5 nm and 10 ms, respectively. All experiments were performed at a sample temperature of 25 °C. We applied protocols that shift the trap between an initial $\lambda(t=0) = 0$ and a final position $\lambda(t_f) = \lambda_f$ within the time interval t_f (see Fig. 1b). After each protocol we waited for the system to fully equilibrate.

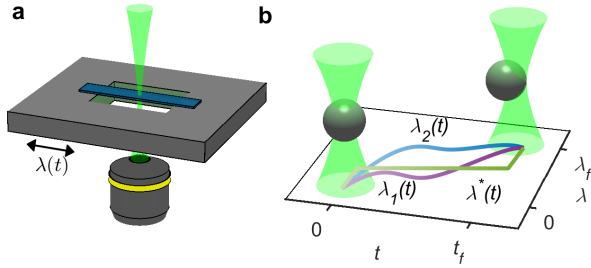


Fig. 1. Principle of an optimal transport experiment. **a**, A colloidal particle is trapped in optical tweezers. Relative movement of the trap center λ is achieved by translating a piezo-actuated sample stage. **b**, The transport protocol $\lambda(t)$ describes the transfer of the trap center from its initial $\lambda(0) = 0$ to its final position λ_f during the time t_f with λ^* corresponding to the protocol of minimal work.

The work W exerted on the particle during such protocols is experimentally determined according to [34, 35]

$$W[\lambda, X] = \int_0^{t_f} \dot{\lambda} \frac{\partial V}{\partial \lambda} dt = \kappa \int_0^{t_f} \dot{\lambda} (\lambda - X) dt. \quad (2)$$

Because W fluctuates between individual protocols due to thermal noise, each measurement was repeated at least 100 times to yield well-defined mean values $\langle W \rangle$. In the following, we determine the optimal transport protocol λ^* which requires the smallest $\langle W \rangle$.

OPTIMAL TRANSPORT IN VISCOUS LIQUIDS

For viscous liquids, the optimal protocol λ^* is known to exhibit symmetric jumps at $t = 0$ and $t = t_f$ and a constant trap velocity in between [1] (see Methods). Such protocols are fully quantified by the jump height $\Delta\lambda$. Figure 2a shows experimental (solid lines) and ideal (dashed lines) protocols for $\Delta\lambda = 0, 0.4$, and $1 \mu\text{m}$ with $\lambda_f = 2 \mu\text{m}$ and $t_f = 1$ s. Since the acceleration of the translational stage is finite, instantaneous jumps cannot be perfectly realized in experiments. Compared to ideal protocols, this leads to deviations at the beginning and the end of $\lambda(t)$ and slightly increases the time during which the optical trap exerts work on the particle. To take this effect into account, when calculating the work (Eq. (2)) the upper integration limit was increased accordingly (see Methods).

Figure 2b shows the experimentally determined mean work $\langle W \rangle$ (black symbols), which exhibits a minimum at $\Delta\lambda^* \approx 0.5 \mu\text{m}$. Despite the above mentioned experimental limitations in realizing ideal jumps, our data are in good agreement with theoretical predictions for protocols with infinitely fast jumps. The predictions are obtained without any adjustable parameters and yield $\Delta\lambda^* = 0.41 \mu\text{m}$ (black line) [1].

Mean particle trajectories x corresponding to the executed protocols are plotted in Fig. 2c. Interestingly, we find that only near the optimal protocol, x obeys time-reversal symmetry, which can be formally written as,

$$f(t) = -f(t_f - t) + f(t_f) \quad (3)$$

with $f \equiv x$. This becomes even clearer when the deviations of x from time-reversal symmetry are quantified. For this purpose we introduce the asymmetry parameter

$$A_f = \frac{1}{t_f} \sum_{t=0}^{t_f/2} [f(t) + f(t_f - t) - 2f(t_f/2)]^2 \Delta t \quad (4)$$

with Δt corresponding to the temporal resolution. A_f is zero for time-symmetric functions f and increases with increasing asymmetry. Figure 2b shows the asymmetry parameter evaluated for $f = x$, A_x , versus $\Delta\lambda$; which exhibits a minimum at the experimentally obtained ideal protocol at $\Delta\lambda^* \approx 0.5 \mu\text{m}$ (symbols). In agreement with the experimental findings, the theoretically predicted trajectories for the perfectly symmetric protocols (with instantaneous jumps) also lead to coinciding minima of $\langle A_x \rangle$ and $\langle W \rangle$.

SYMMETRY PROOF

As will be demonstrated below, the occurrence of time-reversal symmetry of both x^* and λ^* is a distinctive and universal property of a wide class of optimal transport

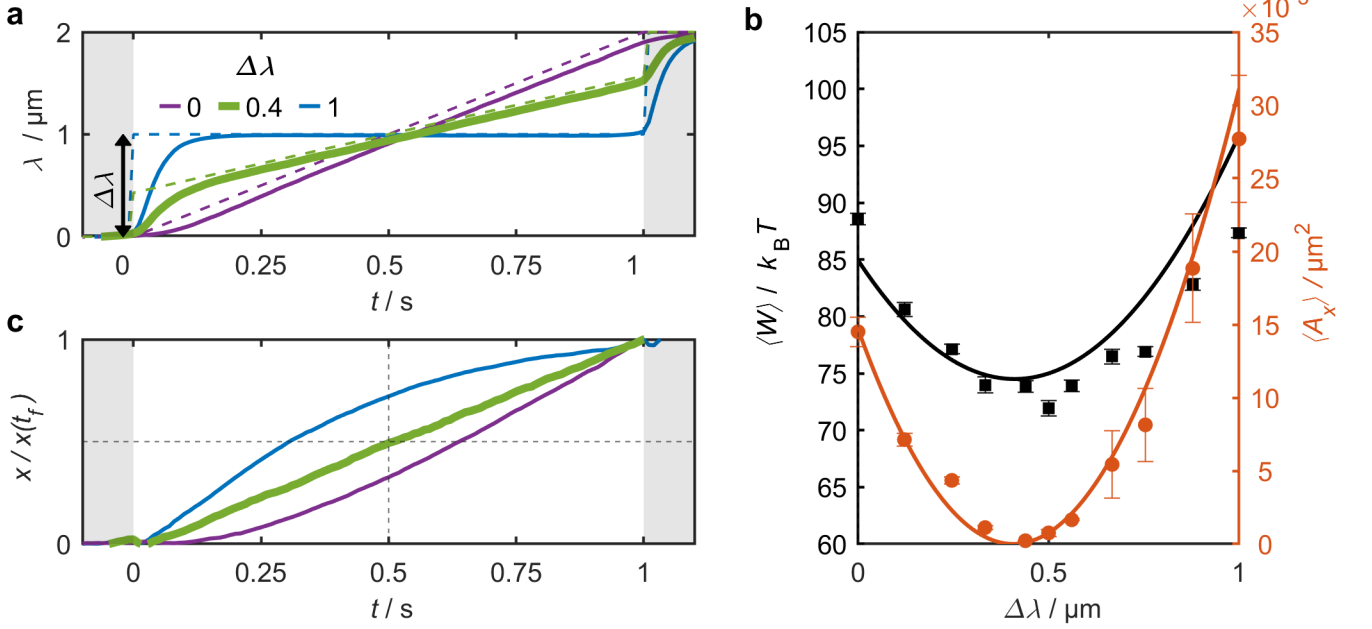


Fig. 2. Optimal transport of a colloidal particle in a viscous fluid. **a**, Experimental (solid lines) protocols for the motion of an optical trap which is displaced by $\lambda_f = 2 \mu\text{m}$ within the time $t_f = 1 \text{ s}$. Different protocols are characterized by their jump height $\Delta\lambda$. The dashed lines correspond to protocols with ideal infinitely fast jumps at start and end of the protocol. The optimal protocol (green) λ^* corresponds to $\Delta\lambda^* = 0.4 \mu\text{m}$ (see Eq. (12) in the Method section). **b**, Experimentally measured mean work $\langle W \rangle$ (black) and asymmetry parameter $\langle A_x \rangle$ (orange) as function of $\Delta\lambda$ (symbols). The minima of $\langle W \rangle$ and $\langle A_x \rangle$ are positioned at the optimal transport protocol λ^* in agreement with theoretical predictions (solid lines). The fact that $\langle A_x \rangle \approx 0$ for λ^* suggests that both λ and x are time symmetric for optimal transport. Error bars correspond to the s.e.m.. **c**, Average particle trajectories x normalized by the position at the end of the protocol $x(t_f)$ corresponding to the protocols shown in **a**.

processes. To prove this surprising observation, we start from a generalized overdamped Langevin equation (GLE) [36–41]

$$\int_{-\infty}^t \Gamma(t-t') \dot{X}(t') dt' = -\nabla V + \nu(t), \quad (5)$$

with an arbitrary memory kernel Γ and zero-mean noise ν . We further assume that the potential V is parabolic (as being the case for an optical trap), rendering the GLE to be linear in X and λ . Notably, no further restrictions are applied to Γ or ν . The latter may also be a colored or a non-Gaussian noise, and we do not restrict to systems obeying the fluctuation-dissipation relation $\Gamma(|t-t'|) \propto \langle \nu(t)\nu(t') \rangle$. Within such assumptions, Eq. (5) describes the dynamics of a broad class of systems, including granular media [28], glasses in their ergodic regime [42, 43], linear viscoelastic fluids [39], polymer condensates [44], particles in bacterial baths [29], and even tracers in molecular fluids [45]. The above GLE also applies to memory-free, viscous liquids by using delta-correlated kernels.

Based on Eq. (5), we obtain general implications and non-implications between optimal transport and time-reversal symmetry of the corresponding protocol λ and

the mean observable (trajectory) x . The results are summarized in Fig. 3. Here, we outline the main idea of the proof, which is described in detail in the Method section.

First, all non-implications can be proved by simple counterexamples (see Methods). For instance, the non-implication *time-reversal symmetry of $\lambda \not\Rightarrow$ time-reversal symmetry of x* becomes immediately obvious by considering an entirely linear protocol $\lambda(t) = (\lambda_f/t_f)t$ which leads in a purely viscous system to an exponentially relaxing trajectory which is clearly not symmetric under time reversal.

Next, by rewriting the work as a functional of either x or λ , only, one can show that optimal transport directly implies time-reversal symmetry. Because the confining potential is quadratic, both in λ and x , the functionals are also quadratic, from which the symmetry directly follows. Concretely, based on Eqs. (2) and (5), the mean work can be expressed as the functional of x

$$\begin{aligned} \langle W \rangle &= \int_0^{t_f} \int_0^t \Gamma(t-t') \dot{x}(t) \dot{x}(t') dt' dt \\ &\quad + \kappa [x(t_f) - \lambda_f]^2 / 2 + \mathcal{C}, \end{aligned} \quad (6)$$

where \mathcal{C} encapsulates terms that are independent of the process during $t \in [0, t_f]$ and therefore irrelevant for the

optimization or symmetry property. To derive Eq. (6) we have further made use of the fact that $\langle W \rangle$ is independent of the noise ν , which is a consequence of the linearity of the GLE. By applying appropriate coordinate transformations, one can show that the functional in Eq. (6) is invariant under time reversal of x , irrespective of the particular memory kernel Γ . Specifically, any trajectory x and its time-reversed image $\tilde{x}(t) \equiv -x(t_f - t) + x(t_f)$ yields the same average work, $\langle W[x] \rangle \equiv \langle W[\tilde{x}] \rangle$. Given the quadratic form of the work functional, we expect only a unique extreme, such that $x^* \equiv \tilde{x}^*$, implying that optimal trajectories are always time-reversal symmetric. Similarly, by explicitly making use of causality of the stochastic process, we can express the mean work as a quadratic functional of $\dot{\lambda}$ convoluted with the response function Φ . Analog arguments then also imply that optimal protocols λ^* must be time-reversal symmetric (Methods).

Finally, to show the reversed implication, we reexamine the work functional (6). Optimal trajectories x^* are characterized by a vanishing variation of the work $\delta\langle W \rangle$ with respect to all variations of x^* that satisfy $\delta x(0) = \delta x(t_f) \equiv 0$. Using variational calculus and some integral manipulations, we find that $\delta\langle W \rangle = 0$, if and only if

$$\frac{d}{dt} \left[\int_0^{t_f} \Gamma(|t - t'|) \dot{x}^*(t') dt' \right] = 0. \quad \forall t \in [0, t_f]. \quad (7)$$

In addition, for all time-symmetric protocols, one can show that any time-symmetric mean solution x of Eq. (5) fulfills the equality

$$\int_0^{t_f} \Gamma(|t - t'|) \dot{x}(t') dt' = \kappa[\lambda_f - x(t_f)]. \quad (8)$$

Realizing that the equality (8) readily implies the condition (7), it follows that $\langle W \rangle$ is optimal whenever x and λ are both time-reversal symmetric.

Overall, we have thus shown that the simultaneous time-reversal symmetry of both x and λ is a necessary and sufficient condition for optimal transport. Importantly, this holds for *all* linear GLE models.

OPTIMAL TRANSPORT IN VISCOELASTIC FLUIDS

To experimentally test the generality of the predicted symmetry and to explore the generic features of optimal transport in non-Markovian environments, we performed transport experiments in a viscoelastic micellar fluid. To realize experimental variations around λ^* , we first obtain a theoretical prediction regarding the optimal protocol. Our calculations are based on previous studies, demonstrating that the memory kernel of micellar viscoelastic solutions is well-described by a single exponential decaying with the bath stress-relaxation time τ_b [23, 39, 44]. As

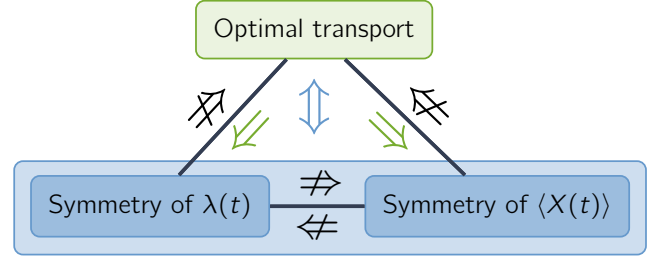


Fig. 3. Universal relations between time-reversal symmetry and optimality. Diagram showing implications (\Rightarrow) and non-implications (\nRightarrow) between time-reversal symmetry (defined in Eq. (3)) of the protocol λ and mean particle trajectory $\langle X \rangle = x$, and optimality with respect to the work required, for transport processes in linear media. Optimal transport is characterized by time-reversal symmetry of both λ and $\langle X \rangle$.

a consequence, the motion of a colloidal particle within such a Maxwell fluid is experimentally observed to be in agreement with two coupled equations [46, 47]

$$\tau_p \dot{X} = -\frac{\kappa}{\kappa_b} (X - \lambda) - (X - X_b) + \xi_p, \quad (9)$$

$$\tau_b \dot{X}_b = -(X_b - X) + \xi_b. \quad (10)$$

Here, X and X_b correspond to the positions of the colloid and a fictitious bath particle connected by a harmonic spring with stiffness κ_b , and ξ_p , ξ_b are Gaussian white noises with variance $2k_B T / \kappa_b^2$, and $\tau_p := \gamma / \kappa_b$.

Expressing the work as functional of $\langle X \rangle$ and $\langle X_b \rangle$ using Eqs. (2) and (9), and incorporating Eq. (10) as dynamical constraint via a Lagrange multiplier, we construct an appropriate cost functional, for which the Euler-Lagrange equations yield x^* , λ^* (see Methods).

The theoretically predicted optimal protocol in a viscoelastic micellar solution is shown as green solid line in Fig. 4b. As expected, λ^* and x^* display time-reversal symmetry (Extended Data). Similar to the Markovian case (even though hardly visible), the optimal protocol exhibits jumps at the beginning and end. However, in non-Markovian systems λ^* contains no linear parts. Only in the quasi-static limit $t_f \rightarrow \infty$ where the memory kernel has decayed to zero the protocol converges to the Markovian case and becomes linear.

To experimentally test the theoretically calculated λ^* , we have varied the protocol around this prediction. Variations around λ^* were achieved by a variation parameter α , with $\alpha = 0.5$ corresponding to λ^* (see Methods). Exemplarily, Fig. 4 shows experimental protocols for three different values of α , all of them exhibiting time-reversal symmetry as suggested by our theoretical considerations. Because the friction in the viscoelastic fluid is larger than that in the viscous water-glycerol mixture, the mean optical trap velocity had to be reduced by setting $\lambda_f = 3 \mu\text{m}$ and $t_f = 10 \text{ s}$. Figure 4c shows the measured averaged

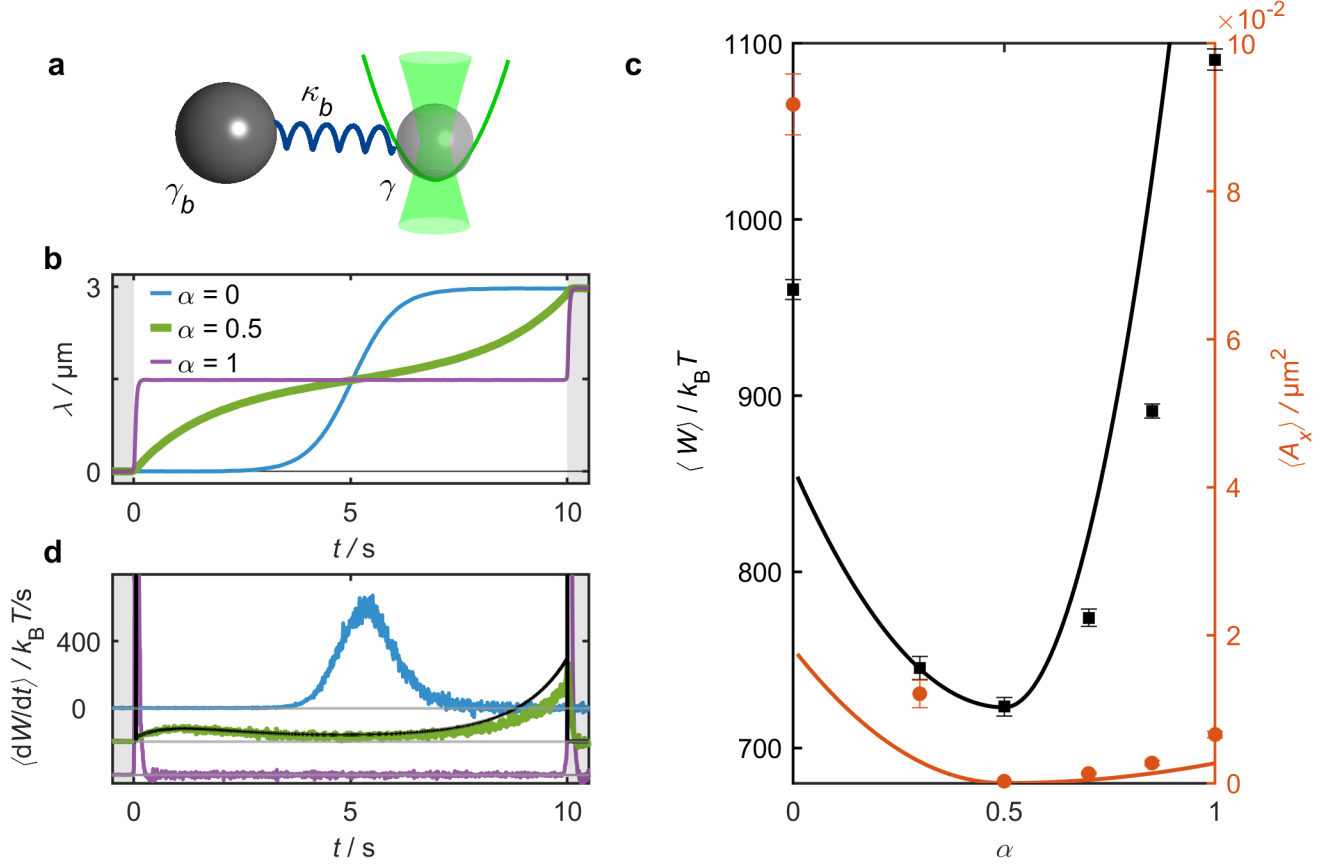


Fig. 4. Optimal transport of a colloidal particle in a viscoelastic fluid. **a**, The sketch visualize the used Maxwell model with fictitious bath particle with friction γ_b , coupled to the tracer particle with friction γ with a linear spring with stiffness κ . Only the tracer feels forces from the optical potential. **b**, Different time-reversal symmetric transport protocols $\lambda(t)$ were executed, which are a linear combination of a tanh-function (blue line), the predicted optimal protocol (green line) and a step-like function (purple line) weighed by a parameter α (for details see Methods). **c** The experimentally measured mean work $\langle W \rangle$ (black symbols) shows a distinct minimum close to $\alpha = 0.5$ that is for the predicted optimal protocol. Theoretical predictions (black line) using the Maxwell model (Eqs. (9),(10)), which are offset by $-290 k_B T$, are in good qualitative agreement with the experimental data. The asymmetric contribution A_x (orange) quantifies the deviation of the mean trajectory x from time-reversal symmetry and exhibits a minimum at the same position as $\langle W \rangle$. Error bars again show the s.e.m.. **d** Measured time resolved power $\langle dW/dt \rangle$ traces for the protocols shown in **b**. Individual protocols are offset to negative values by $200 k_B T$ for better readability, gray lines indicate the corresponding y-axis origin. Protocols including a jump show strong peaks at beginning and end. The work trace for the optimal protocol (green line) shows a complex non-linear and non-monotonic shape. The matching curve from numerically solving the equation of motion (black line) is in good agreement with the experiment.

work $\langle W \rangle$ versus α , indicating a pronounced minimum at $\alpha = 0.5$. In addition, the asymmetry of the mean trajectories $\langle A_x \rangle$ exhibits a minimum for the optimal protocol, which is in excellent agreement with the prediction of time-reversal symmetry of the optimal process independent of the solvent's memory effects.

The appearance of time-reversal symmetry of both λ and x for the optimal solution in non-Markovian systems is particularly astonishing in view of the strongly time-asymmetric nature of the overall process, which starts in thermal equilibrium and ends in a state where the particle within the optical trap and the surrounding are anisotropic and out of equilibrium. This becomes visible in the time-resolved power $\langle dW/dt \rangle$, shown in

Fig. 4c for different time-symmetric protocols and which is clearly not time-symmetric even for λ^* (green curve). In fact, $\langle dW/dt \rangle$ is strongly time-asymmetric and non-monotonic; and the largest contribution to the applied work occurs towards the end of the optimal protocol. This modulated power input differs significantly from the Markovian case, where optimal transport is characterized by constant power between the jumps (see Extended Data Fig. 7).

The nonlinear behavior of λ^* and asymmetry of $\langle dW \rangle$ in a viscoelastic fluid can be rationalized by energetic considerations. At the beginning of the protocol, the fluid is isotropic and fully relaxed. In this regime, the particle can be initially dragged with relatively low energetic

costs even at high trap velocities. With increasing particle displacement, however, the viscoelastic microstructure becomes increasingly distorted, thereby accumulating elastic energy and thus increasing the particle resistance against the trap motion. Therefore, to avoid an excessive increase of work, the trap velocity should be rather slow. However, since the protocol must be completed within t_f , the trap velocity cannot be slow over the entire protocol. This conflict is resolved by slowing down the trap for $t < t_f/2$ and accelerating it afterwards. With this strategy, elastic energy stored in the fluid becomes largest towards the end of the protocol, when the trap has already stopped (at λ_f) and therefore exerts no more work on the particle. We remark that these arguments are in good agreement with the observation that molecular motors modulate their driving in accordance to their resistance [2].

APPLICATION IN MACHINE LEARNING

Finally, we aim to mention an important practical implication of the uncovered symmetry of optimal transport in the context of computational approaches. To demonstrate this, we trained a deep neural network to find the optimal transport protocol in a viscous system [48]. Instead of training the network with the objective of minimizing the work (Fig. 5, black line), we also trained with the objective of minimizing the asymmetries of protocol and mean trajectory $A_x + A_\lambda$ (Fig. 5, orange line). In both cases, the learned protocol converges to the optimal one, demonstrating that the asymmetry parameter can be used as an alternative (or additional) cost functional for the optimization. Moreover, for transport through more complex environments, for which generally no analytical solution is available, the asymmetry parameter offers the essential advantage that its value at the global optimum ($A_x + A_\lambda \equiv 0$) is always and *a priori* known. Therefore, unlike the work, the asymmetry reveals whether the true work optimum has been reached.

CONCLUSION & OUTLOOK

With experiments and theoretical calculations we have studied the optimal transport of a colloidal particle in viscous (memory-free) and viscoelastic (non-Markovian) baths. Despite the very different response of colloidal particles in both systems, we find that the optimal protocols and the corresponding mean particle trajectories always exhibit time-reversal symmetry. Remarkably, such symmetry, which is a hallmark of thermal equilibrium, reappears in these systems far away from equilibrium, when driven in the most energy-efficient way. The symmetry is rather universal and applies to all systems in the regime where the dynamical equations are approximately linear in the system's variable and protocol parameter. It is thus expected to be valid also in underdamped systems,

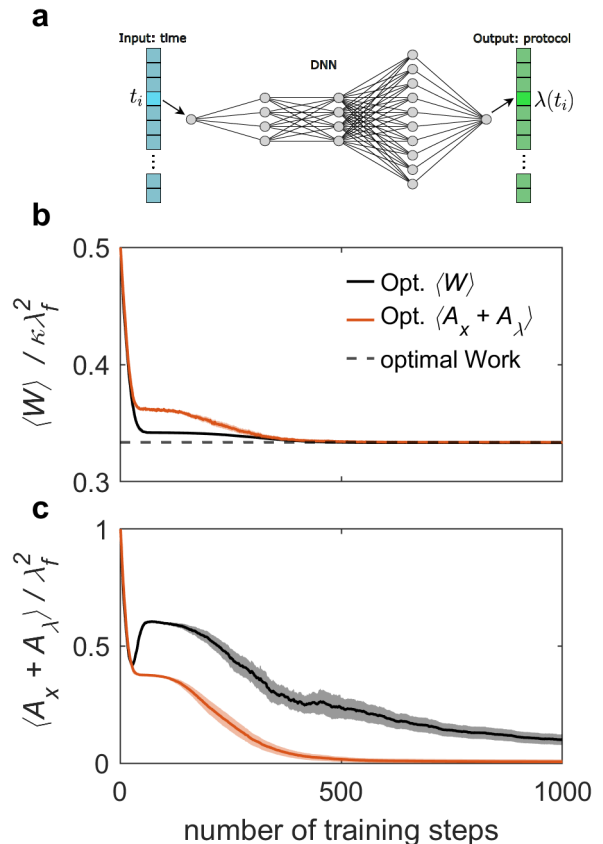


Fig. 5. Optimal protocols with machine learning algorithms trained on asymmetry. We train a deep neural network (DNN) with the objective of minimizing the work $\langle W \rangle$ (black lines), or the overall asymmetry $A_x + A_\lambda$ (orange lines). **b**, Shows the work, **c** shows the total asymmetry during training. The lines depict the averages of 100 independent training runs, the shaded regions indicate standard derivations. Both objectives lead to successful learning. Training on $A_x + A_\lambda$ has the crucial advantage that the globally optimal value $A_x + A_\lambda \rightarrow 0$ is *a priori* known. As illustrated in **a** the network has 5 layers of $\{1, 4, 4, 10, 1\}$ nodes and training is done by a Monte Carlo algorithm, similar to Ref. [48], see Methods for details.

systems with long-ranged memory, such as active fluids [29, 30] or fluids with hydrodynamic backflow [31]. This symmetry property of optimal transport is of immediate relevance for the efficient operation of nanomachines, low energy swimming mechanisms of micro-robotic systems but also energy-efficient information processing [49, 50]. In machine learning, numerical and exact optimization, the *a priori* knowledge of the uncovered time-reversal symmetry provides a strong constraint for the applicable function space and will, thus, significantly improve optimization algorithms.

ACKNOWLEDGMENTS

SL acknowledges funding through the Marie-Curie fellowship (grant ref EP/X031926/1) undertaken by the UKRI, and through the Walter Benjamin Stipendium, project 498288081 from the Deutsche Forschungsgemeinschaft (DFG). CB acknowledges funding through the DFG, Grant No. SFB 1432 - Project ID 4252172. We further thank Mike Cates, Robert Jack, and Édgar Roldán for valuable discussions.

Author contributions

CB, SM and FG designed the experiment. The experimental data were taken and analyzed by SM and dis-

cussed together with FG and CB who supervised the project. SL performed the analytical calculations, derived the theoretical proof and implemented the machine learning model. SL, SM, and CB wrote the manuscript.

Competing Interests

The authors declare no competing interests.

-
- [1] T. Schmiedl and U. Seifert, Optimal finite-time processes in stochastic thermodynamics, *Physical Review Letters* **98**, 108301 (2007).
 - [2] D. A. Sivak and G. E. Crooks, Thermodynamic metrics and optimal paths, *Physical Review Letters* **108**, 190602 (2012).
 - [3] T. Van Vu and K. Saito, Thermodynamic unification of optimal transport: Thermodynamic uncertainty relation, minimum dissipation, and thermodynamic speed limits, *Physical Review X* **13**, 011013 (2023).
 - [4] K. Proesmans, J. Ehrich, and J. Bechhoefer, Finite-time Landauer principle, *Physical Review Letters* **125**, 100602 (2020).
 - [5] J. Li, B. Esteban-Fernández de Ávila, W. Gao, L. Zhang, and J. Wang, Micro/nanorobots for biomedicine: Delivery, surgery, sensing, and detoxification, *Science robotics* **2**, eaam6431 (2017).
 - [6] B. Wang, Y. Zhang, and L. Zhang, Recent progress on micro-and nano-robots: Towards in vivo tracking and localization, *Quantitative imaging in medicine and surgery* **8**, 461 (2018).
 - [7] M. Woods, J. Henderson, and G. Lock, Energy requirements for the flight of micro air vehicles, *The Aeronautical Journal* **105**, 135 (2001).
 - [8] S. Toyabe, T. Watanabe-Nakayama, T. Okamoto, S. Kudo, and E. Muneyuki, Thermodynamic efficiency and mechanochemical coupling of F1-ATPase, *Proceedings of the National Academy of Sciences* **108**, 17951 (2011).
 - [9] R. Grover, J. Fischer, F. W. Schwarz, W. J. Walter, P. Schuille, and S. Diez, Transport efficiency of membrane-anchored kinesin-1 motors depends on motor density and diffusivity, *Proceedings of the National Academy of Sciences* **113**, E7185 (2016).
 - [10] V. Blickle and C. Bechinger, Realization of a micrometre-sized stochastic heat engine, *Nature Physics* **8**, 143 (2012).
 - [11] I. A. Martínez, É. Roldán, L. Dinis, D. Petrov, J. M. Parrondo, and R. A. Roca, Brownian Carnot engine, *Nature Physics* **12**, 67 (2016).
 - [12] T. Schmiedl and U. Seifert, Efficiency at maximum power: An analytically solvable model for stochastic heat engines, *Europhysics Letters* **81**, 20003 (2007).
 - [13] M. Esposito, R. Kawai, K. Lindenberg, and C. Van den Broeck, Efficiency at maximum power of low-dissipation carnot engines, *Physical Review Letter* **105**, 150603 (2010).
 - [14] V. Holubec and A. Ryabov, Cycling tames power fluctuations near optimum efficiency, *Physical review letters* **121**, 120601 (2018).
 - [15] D. Gupta, S. J. Large, S. Toyabe, and D. A. Sivak, Optimal control of the F1-ATPase molecular motor, *The Journal of Physical Chemistry Letters* **13**, 11844 (2022).
 - [16] D. King and J. Roughgarden, Graded allocation between vegetative and reproductive growth for annual plants in growing seasons of random length, *Theoretical Population Biology* **22**, 1 (1982).
 - [17] G. Schiebinger, J. Shu, M. Tabaka, B. Cleary, V. Subramanian, A. Solomon, J. Gould, S. Liu, S. Lin, P. Berube, *et al.*, Optimal-transport analysis of single-cell gene expression identifies developmental trajectories in reprogramming, *Cell* **176**, 928 (2019).
 - [18] T. Caneva, M. Murphy, T. Calarco, R. Fazio, S. Montangero, V. Giovannetti, and G. E. Santoro, Optimal control at the quantum speed limit, *Physical Review Letters* **103**, 240501 (2009).
 - [19] Y. Mao, P. Nielsen, and J. Ali, Passive and active microrheology for biomedical systems, *Frontiers in Bioengineering and Biotechnology* **10**, 10.3389/fbioe.2022.916354 (2022).
 - [20] M. Brust, C. Schaefer, R. Doerr, L. Pan, M. Garcia, P. Arratia, and C. Wagner, Rheology of human blood plasma: Viscoelastic versus Newtonian behavior, *Physical Review Letters* **110**, 078305 (2013).
 - [21] D. Schamel, A. G. Mark, J. G. Gibbs, C. Miksch, K. I. Morozov, A. M. Leshansky, and P. Fischer, Nanopropellers and their actuation in complex viscoelastic media, *ACS nano* **8**, 8794 (2014).
 - [22] Y.-H. Lin, *Polymer viscoelasticity: basics, molecular theories, experiments, and simulations* (World Scientific, 2011).

- [23] H. Rehage and H. Hoffmann, Rheological properties of viscoelastic surfactant systems, *The Journal of Physical Chemistry* **92**, 4712 (1988).
- [24] J. Van der Werff, C. De Kruif, C. Blom, and J. Mellema, Linear viscoelastic behavior of dense hard-sphere dispersions, *Physical Review A* **39**, 795 (1989).
- [25] G. Nägele and J. Bergenholtz, Linear viscoelasticity of colloidal mixtures, *The Journal of chemical physics* **108**, 9893 (1998).
- [26] M. Khan, K. Regan, and R. M. Robertson-Anderson, Optical tweezers microrheology maps the dynamics of strain-induced local inhomogeneities in entangled polymers, *Physical Review Letters* **123**, 038001 (2019).
- [27] X. Cao, D. Das, N. Windbacher, F. Ginot, M. Krüger, and C. Bechinger, Memory-induced Magnus effect, *Nature Physics* **10.1038/s41567-023-02213-1** (2023).
- [28] A. Sarracino, D. Villamaina, G. Gradenigo, and A. Puglisi, Irreversible dynamics of a massive intruder in dense granular fluids, *Europhysics Letters* **92**, 34001 (2010).
- [29] A. Argun, A.-R. Moradi, E. Pinçe, G. B. Bağcı, A. Imparato, and G. Volpe, Non-Boltzmann stationary distributions and nonequilibrium relations in active baths, *Physical Review E* **94**, 062150 (2016).
- [30] O. Granek, Y. Kafri, and J. Tailleur, Anomalous transport of tracers in active baths, *Physical Review Letters* **129**, 038001 (2022).
- [31] T. Franosch, M. Grimm, M. Belushkin, F. M. Mor, G. Foffi, L. Forró, and S. Jeney, Resonances arising from hydrodynamic memory in Brownian motion, *Nature* **478**, 85 (2011).
- [32] S. Burov and E. Barkai, Critical exponent of the fractional langevin equation, *Physical review letters* **100**, 070601 (2008).
- [33] M. Cates and S. Candau, Statics and dynamics of worm-like surfactant micelles, *Journal of Physics: Condensed Matter* **2**, 6869 (1990).
- [34] C. Jarzynski, Nonequilibrium equality for free energy differences, *Physical Review Letters* **78**, 2690 (1997).
- [35] G. E. Crooks, Nonequilibrium measurements of free energy differences for microscopically reversible Markovian systems, *Journal of Statistical Physics* **90**, 1481 (1998).
- [36] R. Kubo, The fluctuation-dissipation theorem, *Reports on progress in physics* **29**, 255 (1966).
- [37] H. Mori, Transport, collective motion, and Brownian motion, *Progress of theoretical physics* **33**, 423 (1965).
- [38] R. Zwanzig, *Nonequilibrium statistical mechanics* (Oxford university press, 2001).
- [39] T. A. Waigh, Microrheology of complex fluids, *Reports on progress in physics* **68**, 685 (2005).
- [40] I. Snook, *The Langevin and generalised Langevin approach to the dynamics of atomic, polymeric and colloidal systems* (Elsevier, 2006).
- [41] T. J. Doerries, S. A. M. Loos, and S. H. L. Klapp, Correlation functions of non-Markovian systems out of equilibrium: Analytical expressions beyond single-exponential memory, *Journal of Statistical Mechanics: Theory and Experiment* **2021**, 033202 (2021).
- [42] H. Cummins, G. Li, Y. Hwang, G. Shen, W. Du, J. Hernandez, and N. Tao, Dynamics of supercooled liquids and glasses: comparison of experiments with theoretical predictions, *Zeitschrift für Physik B Condensed Matter* **103**, 501 (1997).
- [43] L. F. Elizondo-Aguilera and T. Voigtmann, Glass-transition asymptotics in two theories of glassy dynamics: Self-consistent generalized Langevin equation and mode-coupling theory, *Physical Review E* **100**, 042601 (2019).
- [44] L. Jawerth, E. Fischer-Friedrich, S. Saha, J. Wang, T. Franzmann, X. Zhang, J. Sachweh, M. Ruer, M. Ijavi, S. Saha, *et al.*, Protein condensates as aging maxwell fluids, *Science* **370**, 1317 (2020).
- [45] A. V. Straube, B. G. Kowalik, R. R. Netz, and F. Höfling, Rapid onset of molecular friction in liquids bridging between the atomistic and hydrodynamic pictures, *Communications Physics* **3**, 126 (2020).
- [46] J. Caspers, N. Ditz, K. Krishna Kumar, F. Ginot, C. Bechinger, M. Fuchs, and M. Krüger, How are mobility and friction related in viscoelastic fluids?, *The Journal of Chemical Physics* **158**, 024901 (2023).
- [47] F. Ginot, J. Caspers, L. F. Reinalter, K. K. Kumar, M. Krüger, and C. Bechinger, Recoil experiments determine the eigenmodes of viscoelastic fluids, *arXiv preprint arXiv:2204.02369* (2022).
- [48] S. Whitelam, Demon in the machine: learning to extract work and absorb entropy from fluctuating nanosystems, *Physical Review X* **13**, 021005 (2023).
- [49] S. Dago, S. Ciliberto, and L. Bellon, Adiabatic computing for optimal thermodynamic efficiency of information processing, *arXiv preprint arXiv:2302.09957* (2023).
- [50] K. Proesmans, J. Ehrich, and J. Bechhoefer, Optimal finite-time bit erasure under full control, *Physical Review E* **102**, 032105 (2020).
- [51] J. Gieseler, J. R. Gomez-Solano, A. Magazzu, I. P. Castillo, L. P. Garcia, M. Gironella-Torrent, X. Viader-Godoy, F. Ritort, G. Pesce, A. V. Arzola, K. Volke-Sepulveda, and G. Volpe, Optical tweezers - from calibration to applications: a tutorial, *Advances in Optics and Photonics* **13**, 74 (2021).
- [52] D. Blair and E. Dufrense, <https://site.physics.georgetown.edu/matlab/index.html> (2005).
- [53] M. Toda, R. Kubo, N. Saitō, and N. Hashitsume, *Statistical physics II: nonequilibrium statistical mechanics*, Vol. 2 (Springer Science & Business Media, 1991).
- [54] P. Nazé, S. Deffner, and M. V. S. Bonança, Optimal finite-time processes in weakly driven overdamped Brownian motion, *Journal of Physics Communications* **6**, 083001 (2022).
- [55] O. Paredes-Altuve, E. Medina, and P. J. Colmenares, Extracting work from a single reservoir in the non-Markovian underdamped regime, *Physical Review E* **94**, 062111 (2016).

METHODS

Model and optimal transport through viscous fluid

The dynamics of the particle in the harmonic trap of stiffness κ in the viscous fluid is described very accurately by the Markovian overdamped Langevin equation

$$\tau_0 \dot{X} = -(X - \lambda) + \xi \quad (11)$$

with zero-mean, Gaussian white noise ξ with $\langle \xi(t) \xi(t') \rangle = 2k_B T \tau_0 \delta(t - t')$, where $\tau_0 = \gamma_0 / \kappa$ denotes the relaxation

time in the trap, and γ_0 is the friction constant. The seminal paper [1] showed that the optimal protocol in this case has at the beginning ($t = 0$) and end ($t = t_f$) two symmetric jumps of size $\Delta\lambda^* = m^*\tau_0$, and is linear in between with slope $m^* = \lambda_f/(t_f + 2\tau_0)$,

$$\lambda^*(t) = \begin{cases} 0, & t = 0 \\ m^*(\tau_0 + t), & 0 < t < t_f \\ \lambda_f, & t = t_f \end{cases} \quad (12)$$

The corresponding optimal trajectories are fully linear: $x^*(t) = m^*t$, and the optimal mean work takes the value $\langle W^* \rangle = \gamma_0 \lambda_f^2 / (t_f + 2\tau_0)$. Thus, in the viscous fluid, optimal transport is achieved, when particle and trap both exhibit a motion of the same constant speed m^* for $0 < t < t_f$, akin a steady state. In order to initiate this joint constant-speed motion, the trap needs to abruptly jump at time $t = 0$, bringing the particle to the displacement from the trap center, where the relaxation force is constant and balanced with the trap's speed.

Optical Trap Setup

The optical tweezers setup used consists of a 532 nm laser (Coherent Verdi V2) that is amplitude modulated with an acousto-optic deflector (AOD, AA optoelectronics DTSXY-400). The laser power in front of the AOD was adjusted to 250 mW using a $\lambda/2$ -plate and a polarizing beam splitter. As a result the laser power after the AOD remained below 100 mW. A 100x objective (Olympus Apochromat MPLAPON-Oil 100x NA=1.45) was used to focus the laser beam onto the sample cell. To manipulate the sample position a 3-axis piezo stage (piezoconcept LT3) was used. Its position was controlled using the analog input with a signal supplied with a sampling rate of 5 kHz by a PCIe card (National Instruments PCIe-6351). At the same time the actual position of the stage was measured from the analog output signal. Differences between the set and actual positions occur when the stage position is adjusted fast. The sample temperature was controlled by resistive heating of the sample stage and microscope objective (Okolab). The temperature was kept at 25°C throughout all experiments. For video microscopy the same microscope objective was used to give an image on a digital camera (Basler ace 2 a2A3840-45umPRO). Videos were acquired during the experiment at a frame rate of 100 frames per second.

Sample preparation

The viscoelastic solution was prepared by dissolving equimolar amounts of cetylpyridinium chloride monohydrate (CPyCl) and sodium salicylate (NaSal) in milipor water. The solution was stirred over night to ensure equilibration of the micellar network. In this study we

used a 8 mM solution.

Sample solutions were prepared by dispersing colloids (2.73 μm SiO₂, micro particles GmbH) in either the water-glycerol mixture or the viscoelastic solution using an ultrasonic bath. Samples were prepared by filling glass capillaries with an inner diameter of 100 μm (CM Scientific) with the sample solution. The capillaries were closed with a combination of wax and epoxy resin. After filling the capillary the samples were equilibrated in the measurement setup until the measured mean work shows no drift anymore.

Measurement Procedures

All protocols consist of moving the trap center λ according to a specific protocol over a distance λ_f in a time t_f . The trap stiffness κ remains constant. Translation of the trap center was technically realized by translating the sample relative to static trap. In a single measurement run, the protocol was executed in both the forward and backward directions consecutively, ultimately ending up in the same trap position. Before and after each individual protocol, the system was allowed to relax for a specified time interval t_{rel} . The trap stiffness was extracted from equilibrium measurements done beforehand.

Variation of Optimal Protocols

To investigate the optimality of protocols predicted by theory in experiments, the protocols were systematically varied as a function of one order parameter.

Viscous Case

For the (Markovian) case of a particle in a viscous fluid, the optimal protocol for the shifting of a trap center in a finite time is given by Eq. (12). The optimal protocol has symmetric jumps of height $\Delta\lambda^*$ at the beginning and end. It can be seen as a member of the family of functions described by

$$\lambda(0 < t < t_f) = m t + \Delta\lambda, \quad (13)$$

$$m = \frac{\lambda_f - \Delta\lambda}{t} \quad (14)$$

To check the optimality of λ^* , protocols defined by Eq. (13) with varying $\Delta\lambda^*$ were executed. To keep the overall symmetry of the protocol, the slope of the linear part of the protocol m is adjusted according to Eq. (14).

To calculate a prediction for the optimal jump height $\Delta\lambda^*$, it is necessary to know the relaxation time of the particle in the trap τ_0 . The latter is given as the quotient of particle friction γ_0 and trap stiffness κ , both of which can be determined from equilibrium measurements [51]. The trap stiffness κ was extracted by fitting a parabolic function to the potential derived from the equilibrium distribution using the Boltzmann factor. Using the derived trap stiffness, the friction coefficient γ_0 was subsequently derived from initial slope of the mean square displacement (see Extended Data, Fig. 6). The final result was $\tau_0 = 0.3475$ s.

Viscoelastic Case

The optimal protocol for the viscoelastic solution, i.e., the non-Markovian case, is more complex. It was calculated exactly from Eq. (60) using Mathematica. In order to perform the calculation of the protocol in addition to λ_f and t_f , the parameters γ , γ_b , κ_b and k , which define the system dynamics according to the set of overdamped LEs (Eqs. (9), (10)), need to be known. To determine the three system parameters γ , γ_b and κ_b , we first conducted test experiments, before the actual experiments, with protocols having a constant trap velocity λ_f/t_f . The average performed work $\langle W_{\text{exp}} \rangle$ was compared with corresponding simulations considering a single bath particle model. The difference in average work between simulation and experiment were minimized using a gradient descent algorithm which adjusts γ , γ_b and κ_b . To generate a protocol variation in dependence of a single parameter (like in the Markovian case), we constructed a superposition of different protocols. Concretely, we used protocols that are a linear combination of a tanh-function (λ_T , Eq. (16)), the optimal protocol (λ^* , Eq. (60)), and a step function featuring two symmetric jumps at the beginning and the end (λ_S , Eq. (17)). To generate an individual test protocol for an experiment, the three base functions are mixed using a linear weighing approach as a function of the mixing parameter α , as given in Eq. (15):

$$\lambda(t) = w_T \lambda_T(t) + w_S \lambda_S(t) + w_O \lambda^*(t), \quad (15)$$

$$\lambda_T(t) = \frac{\lambda_f}{2} \left[\tanh\left(t - \frac{t_f}{2}\right) + 1 \right], \quad (16)$$

$$\lambda_S(t) = \begin{cases} 0 & \text{for } \tau < 0 \\ \lambda_f/2 & \text{for } 0 \leq \tau < t_f \\ \lambda_f & \text{for } \tau \geq t_f \end{cases}, \quad (17)$$

$$w_O = 1 - |2\alpha - 1|, \quad (18)$$

$$w_T = \max(1 - 2\alpha, 0), \quad (19)$$

$$w_S = \max(2\alpha - 1, 0). \quad (20)$$

By varying the mixing parameter, the individual contributions can be controlled, with $\alpha = 0$ representing a tanh function, $\alpha = 0.5$ corresponding to the optimal protocol,

and $\alpha = 1$ corresponding to the step function. In between these edge cases, the protocols are superpositions of the two respective functions.

Data Evaluation

The particle position is tracked by analyzing video recordings captured at a frame rate of 100 fps using a custom tracking algorithm based on Ref. [52]. The position of the piezo stage and the exposure active signal of the camera are recorded at 5 kHz using a PCIe card. Using this data stage and particle data are synchronized *a posteriori*.

The work done during an individual protocol is calculate from in the framework of stochastic thermodynamics using Stratonovich integrals (see Eq. (2)). Since the trajectory is only sampled at finite intervals $\Delta t = 0.01$ s the integral transforms into a sum:

$$W = \sum_{i=1}^{N-1} \frac{\frac{\partial V}{\partial \lambda}|_{t_{i+1}} + \frac{\partial V}{\partial \lambda}|_{t_i}}{2} \left(\lambda(t_{i+1}) - \lambda(t_i) \right). \quad (21)$$

The calculated work was then averaged over multiple trajectories.

Due to the inertia of the stage, it did not reach its final position λ_f at $t_f = 10$ s but only about 0.1 s later. To account for this contribution to the work the time frame of work calculation was extended until $\dot{\lambda} \approx 0$. Similar considerations must be done for the asymmetry parameter A_x : The increased protocol time shifts the inflection point of the symmetry operation to slightly later times. To account for this the time frame for calculating A_x was extended to t'_f so that the observed inflection point lies at $t'_f/2$. For this adjusted integration window, the asymmetry parameter of the protocol A_λ is minimal.

Counterexamples to show non-implications between symmetries and optimality

Here we briefly show all non-implications sketched in Fig. 3, by giving two counterexamples. To this end, we consider the case of a particle in a viscous fluid. First, while a fully linear protocol $\lambda(t) = (\lambda_f/t_f)t$ possesses time-reversal symmetry, the corresponding mean particle trajectory violates it. This is seen in Fig. 2 (b), case $\Delta\lambda = 0$ (purple curve), consistent with the theoretical prediction obtained by solving the LE (11) for the linear protocol, which predicts an exponential relaxation in the comoving reference frame: $x(t) = (\lambda_f/t_f)[t - \tau_0(1 - e^{-t/\tau_0})]$. Here, $\tau_0 := \gamma_0/\kappa$ denotes the trap relaxation time, and γ_0 the friction coefficient. Thus *symmetry of $\lambda \not\Rightarrow$ symmetry of x* . This counterexample also demonstrates that *symmetry of $\lambda \not\Rightarrow$ minimal $\langle W \rangle$* . As a second counterexample, consider the protocol

$\lambda(0) = 0$, $\lambda(t > 0) = m'(\tau_0 + t)$ with $m' = \lambda_f/(t_f + \tau_0)$, which has a single jump at $t = 0$ and no jump at time t_f , and thus violates time-reversal symmetry. However, the corresponding mean trajectory is given by $x(t) = m't$, and is thus time-symmetric; showing that *symmetry of x \nRightarrow symmetry of λ* , and that *symmetry of x \nRightarrow minimal $\langle W \rangle$* .

Proof of: optimality \Rightarrow symmetry of x

Here we provide more details of the proof that optimality implies time-reversal symmetry of x . As a first step, we express the work as a functional of x only. To this end, we first simplify Eq. (2) by explicit integration of $\dot{\lambda}$ and a partial integration of $\dot{\lambda}X$, taking into account the boundary conditions, which yields

$$W[\lambda, X] = \kappa \left[\frac{\lambda_f^2}{2} - X(t_f)\lambda_f \right] + \kappa \int_0^{t_f} \lambda(t)\dot{X}(t)dt. \quad (22)$$

Next, substituting λ by

$$\lambda(t) = \kappa^{-1} \int_{-\infty}^t \Gamma(t-t')\dot{X}(t')dt' + X(t) - \kappa^{-1}\nu(t), \quad (23)$$

which follows from solving the GLE (5) for λ , and taking the noise average, we find the functional

$$\begin{aligned} \langle W \rangle[x] = & (\kappa/2) \langle [\lambda_f - X(t_f)]^2 \rangle - (\kappa/2) \langle X(0)^2 \rangle \\ & + \int_{-\infty}^{t_f} \int_0^t \Gamma(t-t') \langle \dot{X}(t)\dot{X}(t') \rangle dt' dt, \end{aligned} \quad (24)$$

where we have used that $\langle \nu(t) \rangle = 0$. Note that the first two terms are the increase of potential energy from time 0 to t_f . To proceed further, we make use of the fact that the mean work is independent of the noise. To make this apparent, we average over Eq. (2), which yields $\langle W \rangle = \kappa \int_0^{t_f} \dot{\lambda}(\lambda - x)dt$. Noting that, due to the linearity of the GLE, the temporal evolution of x is independent of the noise, we conclude that the same holds for $\langle W \rangle$. Thus, we are allowed to evaluate Eq. (24) in the noise-free limit, where $\langle \dot{X}(t)\dot{X}(t') \rangle \rightarrow \dot{x}(t)\dot{x}(t')$. Finally, we encapsulate in the constant \mathcal{C} all terms of Eq. (24) that are independent of the process during $t \in [0, t_f]$ (and thus play no role in the optimization), allowing us to tighten the bounds of integration, and leading to

$$\begin{aligned} \langle W \rangle[x] = & \int_0^{t_f} \int_0^t \Gamma(t-t')\dot{x}(t)\dot{x}(t')dt' dt \\ & + (\kappa/2)[x(t_f) - \lambda_f]^2 + \mathcal{C}, \end{aligned} \quad (25)$$

as given in Eq. (6) in the main text.

This functional is invariant under time reversal. To show this, we first consider only the integral term of $\langle W \rangle[x]$ and perform the coordinate transformations $t' = t_f - t''$, and $t = t_f - \tilde{t}$, which leads to

$$\begin{aligned} & \int_0^{t_f} \int_0^t \Gamma(t-t')\dot{x}(t')\dot{x}(t)dt'dt \\ & = \int_0^{t_f} \int_{\tilde{t}}^{t_f} \Gamma(t'' - \tilde{t})\dot{x}(t_f - t'')\dot{x}(t_f - \tilde{t})d\tilde{t}dt''. \end{aligned} \quad (26)$$

Now, interchanging the order of integration and accordingly adjusting the limits of the double-integral [53],

$$\dots = \int_0^{t_f} \int_0^{t''} \Gamma(t'' - \tilde{t})\dot{x}(t_f - t'')\dot{x}(t_f - \tilde{t})d\tilde{t}dt'', \quad (27)$$

and subsequently renaming $t'' \rightarrow t$ and $\tilde{t} \rightarrow t'$, we find

$$\dots = \int_0^{t_f} \int_0^t \Gamma(t-t')\dot{x}(t_f - t)\dot{x}(t_f - t')dt'dt. \quad (28)$$

Comparing this with the original integral in Eq. (25) [or equivalently, Eq. (6) in the main text], we notice that each path x and its time-reversed image $\hat{x}(t) \equiv \pm x(t_f - t) + \mathcal{C}_s$, with some arbitrary constant \mathcal{C}_s , give the same value of the integral term. However, among the possible $\hat{x}(t)$, only the one with $\mathcal{C}_s = x(t_f)$ and negative sign of the $x(t_f - t)$ term, is compatible with the equilibrium initial condition, and satisfies $\hat{x}(t_f) = x(t_f)$, such that the remaining contribution to $\langle W \rangle[x]$ in Eq. (25) is also identical for \hat{x} and x . We conclude that any given trajectory $x(t)$ and its time-reversed image $\hat{x}(t) = -x(t_f - t) + x(t_f)$ yield the same work. Since the work can be expressed as a quadratic functional of x alone (see Eq. (25)), we expect only a unique optimum, such that optimal trajectories must satisfy $x^* \equiv \hat{x}$ and consequentially possess time-reversal symmetry.

Proof of: optimality \Rightarrow symmetry of λ

Here, we outline the proof of that optimal protocols λ^* are time-symmetric. First, we show how one can generally express x as functional of λ . To this end, we take the noise average of the GLE (5), which, together with the equilibrium initial condition, yields

$$\int_0^t \Gamma(t-t')\dot{x}(t')dt' = -\kappa[x(t) - \lambda(t)]. \quad (29)$$

To formally solve Eq. (29) for x , we apply a Laplace transformation, $\hat{f}(s) = \int_0^\infty f(t)e^{-st}dt$, and make use of the convolution theorem, obtaining

$$\begin{aligned} \hat{\Gamma}(s)\hat{x}(s) & = -\kappa\hat{x}(s) + \kappa\hat{\lambda}(s) \\ \Leftrightarrow \hat{\Gamma}(s)[s\hat{x}(s) - x(0)] & = -\kappa\hat{x}(s) + \kappa\hat{\lambda}(s). \end{aligned} \quad (30)$$

Recalling $x(0) = 0$ and solving for $\hat{x}(s)$, we find

$$\hat{x}(s) = \hat{\Phi}(s) s \hat{\lambda}(s), \quad (31)$$

with the response function in Laplace domain

$$\hat{\Phi}(s) := \frac{\kappa}{\hat{\Gamma}(s) + s^{-1}\kappa}. \quad (32)$$

Noting that $\lambda(0) = 0$ and thus $s\hat{\lambda}(s) = [s\hat{\lambda}(s) - \lambda(0)]$, we transform back to the time domain, and find

$$x(t) = \int_0^\infty \Phi(t-t') \dot{\lambda}(t') dt'. \quad (33)$$

Assuming causality of the stochastic process implies that any response function must satisfy $\Phi(t < 0) = 0$, so that we can tighten the integration limits and finally find

$$x(t) = \int_0^t \Phi(t-t') \dot{\lambda}(t') dt'. \quad (34)$$

Now, this expression can be used to replace x in the noise-average of Eq. (2), directly leading to the following expression of the work as a functional of λ only,

$$\langle W \rangle [\lambda] = \frac{\kappa \lambda_f^2}{2} + \kappa \int_0^{t_f} \int_0^t \Phi(t-t') \dot{\lambda}(t) \dot{\lambda}(t') dt' dt. \quad (35)$$

Starting from this functional, which is again quadratic in λ , and repeating the analogous steps as we have used before to prove time-reversal symmetry of x^* , readily implies that λ^* possesses time-reversal symmetry, too. Consistent with our findings, it was shown in Ref. [54] using linear response theory that optimal protocols of generic Hamiltonian systems in the fast-but-weak driving regime are time-symmetric.

Proof of: symmetry of x and $\lambda \Rightarrow$ optimality

Finally, we show that the combined symmetry of x and λ implies that the process is optimal. The main step of this proof is to derive a generic condition on x for optimality via variational calculus (leading to Eq. (7) given in the main text).

To this end, we start from the work functional given in Eq. (6). The variation of $\langle W \rangle[x]$ with respect to variations of x that satisfy $\delta x(0) = \delta x(t_f) = 0$ is generally given by

$$\begin{aligned} \delta \langle W \rangle [x(t), \delta x(t)] &= \int_0^{t_f} \int_0^t \Gamma(t-t') \dot{x}(t') \delta \dot{x}(t) dt' dt \\ &+ \int_0^{t_f} \int_0^t \Gamma(t-t') \delta \dot{x}(t') \dot{x}(t) dt' dt, \end{aligned} \quad (36)$$

The second term of this last expression can be rewritten, by interchanging the integrals,

$$\int_0^{t_f} \int_0^t \Gamma(t-t') \delta \dot{x}(t') \dot{x}(t) dt' dt \quad (37)$$

$$= \int_0^{t_f} \int_{t'}^{t_f} \dot{x}(t) \Gamma(t-t') \delta \dot{x}(t') dt dt'. \quad (38)$$

and renaming $t \rightarrow t'$, $t' \rightarrow t$,

$$\dots = \int_0^{t_f} \int_t^{t_f} \dot{x}(t') \Gamma(t'-t) \delta \dot{x}(t) dt' dt. \quad (39)$$

Now, by using twice the identity: $a = |a|$, $\forall a > 0$, we can combine both integral terms of $\delta \langle W \rangle$ from Eq. (36), and find

$$\delta \langle W \rangle = \int_0^{t_f} \delta \dot{x}(t) \int_0^{t_f} \Gamma(|t-t'|) \dot{x}(t') dt' dt. \quad (40)$$

Finally, integration by parts and using that, per definition, $\delta x(0) = \delta x(t_f) = 0$, yields

$$\delta \langle W \rangle = \int_0^{t_f} \delta x(t) \frac{d}{dt} \left[\int_0^{t_f} \Gamma(|t-t'|) \dot{x}(t') dt' \right] dt. \quad (41)$$

Thus, trajectories that satisfy the condition

$$\frac{d}{dt} \left[\int_0^{t_f} \Gamma(|t-t'|) \dot{x}(t') dt' \right] = 0. \quad \forall t \in [0, t_f] \quad (42)$$

automatically fulfill $\delta \langle W \rangle [x(t), \delta x(t)] = 0$ for all variations with $\delta x(0) = \delta x(t_f) = 0$, which is a characteristic property of optimal solutions.

For sake of completeness, we note that, starting from Eq. (35), analogous steps yield the analogous condition

$$\frac{d}{dt} \left[\int_0^{t_f} \Phi(|t-t'|) \dot{\lambda}(t') dt' \right] = 0. \quad \forall t \in [0, t_f], \quad (43)$$

for optimal protocols.

The second step of this proof is to show that symmetric transport processes automatically satisfy the condition (42) (which is identical to Eq. (7) given in the main text). We start with assuming that a given protocol is time-symmetric, i.e.,

$$\lambda_f = \lambda(t) + \lambda(t_f - t). \quad (44)$$

Substituting in this equation $\lambda(t)$ and $\lambda(t_f - t)$ using the noise-averaged GLE (29), yields

$$\begin{aligned} \lambda_f &= \frac{1}{\kappa} \int_0^t \Gamma(t-t') \dot{x}(t') dt' + x(t) \\ &+ \frac{1}{\kappa} \int_0^{t_f-t} \Gamma(t_f-t-t') \dot{x}(t') dt' + x(t_f-t). \end{aligned} \quad (45)$$

Now, transforming the coordinates of the second integral ($t' = t_f - t''$) and assuming that the trajectory x also possesses time-reversal symmetry, we find

$$\begin{aligned} \kappa[\lambda_f - x(t_f)] &= \int_0^t \Gamma(t - t') \dot{x}(t') dt' \\ &+ \int_t^{t_f} \Gamma(t'' - t) \dot{x}(t_f - t'') dt''. \end{aligned} \quad (46)$$

Finally, using $\dot{x}(t_f - t) = \dot{x}(t)$ which is implied by the time-reversal symmetry of x , and again the identity: $a = |a|$, $\forall a > 0$, we find

$$\begin{aligned} \kappa[\lambda_f - x(t_f)] &= \int_0^t \Gamma(|t - t'|) \dot{x}(t') dt' \\ &+ \int_t^{t_f} \Gamma(|t - t''|) \dot{x}(t'') dt'' \end{aligned} \quad (47)$$

which readily implies

$$\int_0^{t_f} \Gamma(|t - t'|) \dot{x}(t') dt' = \kappa[\lambda_f - x(t_f)], \quad (48)$$

as given in Eq. (8) in the main text. It is easy to see that this equality, which is fulfilled by all processes with time-symmetric x and λ , readily implies that condition (42) is fulfilled. This further implies that time-symmetric processes are generally optimal.

Calculation of optimal protocol for viscoelastic fluid

Here, we derive the optimal protocols for the particle in a Maxwell fluid described by the GLE (5) with $\Gamma(t - t') = 2\gamma\delta(t - t') + \kappa_b e^{-(t-t')/\tau_b}$, and $\langle \nu(t)\nu(t') \rangle = 2k_B T [\gamma\delta(\Delta t) + \gamma_b e^{-|\Delta t|/\tau_b}]$, with the bath stress-relaxation time τ_b . Equivalently, the dynamics of X can be described by Eqs. (9) and (10), as given in the main text.

As a first step, we express the work as a functional of x and $x_b := \langle X_b \rangle$, only. To this end, we use the noise average of Eqs. (9) and (10), which is

$$\tau_p \dot{x} = -(k+1)x + x_b + k\lambda, \quad (49)$$

$$\tau_b \dot{x}_b = -x_b + x. \quad (50)$$

Solving Eq. (49) for λ and substituting the result, we can rewrite Eq. (2) as

$$\begin{aligned} \langle W \rangle[x, x_b] &= \frac{\kappa}{k^2} \int_0^{t_f} dt [\tau_p^2 \ddot{x} \dot{x} + \tau_p \ddot{x} x - \tau_p \ddot{x} x_b - \tau_p \dot{x} \dot{x}_b \\ &+ \tau_p(k+1)\dot{x}^2 + (k+1)\dot{x}x - (k+1)\dot{x}x_b \\ &- x\dot{x}_b + \dot{x}_b x_b]. \end{aligned} \quad (51)$$

This can be simplified by explicitly integrating all terms of the form $\int_0^{t_f} \dot{x} x dt = \frac{1}{2}[x^2]_0^{t_f}$, and rewriting by partial integration some of the other terms like $\int_0^{t_f} \dot{x} x_b dt = \frac{1}{2}[x x_b]_0^{t_f} - \int_0^{t_f} x \dot{x}_b dt$; leading to

$$\begin{aligned} \frac{k}{\kappa} \langle W \rangle[x, x_b] &= \int_0^{t_f} dt (\tau_p \dot{x}^2 - \dot{x} x_b) \\ &+ \frac{1}{2k} [\tau_p^2 \dot{x}^2 + (k+1)x^2 + x_b^2]_0^{t_f} \\ &+ \frac{1}{k} [\tau_p \dot{x} x - \tau_p \dot{x} x_b - x x_b]_0^{t_f}. \end{aligned} \quad (52)$$

Next, to minimize the work functional (52), we incorporate as a constraint the noise-averaged Eq. (10) via a Lagrange multiplier $\Lambda(t)$, giving rise to the cost functional (Lagrangian)

$$\mathcal{L}[x, \dot{x}, \dot{x}_b] = [\tau_p \dot{x}^2 - \dot{x} x_b] + \Lambda(t)[\tau_b \dot{x}_b + x_b - x]. \quad (53)$$

For this cost functional, the Euler-Lagrange equations

$$\frac{\partial \mathcal{L}}{\partial x} - \frac{d}{dt} \frac{\partial \mathcal{L}}{\partial \dot{x}} = 0, \quad (54)$$

$$\frac{\partial \mathcal{L}}{\partial x_b} - \frac{d}{dt} \frac{\partial \mathcal{L}}{\partial \dot{x}_b} = 0, \quad (55)$$

yield the set of two linear, coupled second-order differential equations: $2\tau_p \ddot{x} = \dot{x}_b - \Lambda$ and $\tau_b \ddot{\Lambda} = -\dot{x} + \Lambda$. Introducing the variable $v := \dot{x}$, and explicitly inserting the dynamical constraint (50), i.e., the noise-averaged Eq. (10), we can write the latter as the set of four coupled linear, first-order differential equations

$$\dot{\mathbf{z}} = \mathbb{A} \mathbf{z}, \quad \text{with} \quad \mathbf{z} = (x \ v \ x_b \ \Lambda)^T, \quad (56)$$

$$\mathbb{A} = \begin{pmatrix} 0 & 1 & 0 & 0 \\ \frac{1}{2\tau_b\tau_p} & 0 & -\frac{1}{2\tau_b\tau_p} & -\frac{1}{2\tau_p} \\ \frac{1}{\tau_b} & 0 & -\frac{1}{\tau_b} & 0 \\ 0 & -\frac{1}{\tau_b} & 0 & \frac{1}{\tau_b} \end{pmatrix}. \quad (57)$$

The solution of this equation is $\mathbf{z} = \mathbf{z}(0)e^{\mathbb{A}t}$. In combination with the initial conditions $x(0) = 0, x_b(0) = 0$, this yields the optimal solution

$$x^*(t) = \frac{1}{2(\tau_b + \tau_p)} \left[2\tau_p \mathcal{C}_1 t + \tau_b(\tau_b + t)\mathcal{C}_2 + \tau_b^2 \left\{ -\mathcal{C}_2 \cosh \frac{\sqrt{\tau_b + \tau_p}}{\tau_b \sqrt{\tau_p}} t + \frac{\sqrt{\tau_p}(2\mathcal{C}_1 - \mathcal{C}_2)}{\sqrt{\tau_b + \tau_p}} \sinh \frac{\sqrt{\tau_b + \tau_p}}{\tau_b \sqrt{\tau_p}} t \right\} \right] \quad (58)$$

$$x_b^*(t) = \frac{1}{2(\tau_b + \tau_p)} \left[2\tau_p \mathcal{C}_1 + \tau_b \mathcal{C}_2 + \tau_b(2\mathcal{C}_1 - \mathcal{C}_2) \cosh \frac{\sqrt{\tau_b + \tau_p}}{\tau_b \sqrt{\tau_p}} t - \tau_b \frac{\sqrt{\tau_b + \tau_p}}{\sqrt{\tau_p}} \sinh \frac{\sqrt{\tau_b + \tau_p}}{\tau_b \sqrt{\tau_p}} t \right] \quad (59)$$

$$\lambda^*(t) = \frac{1}{2(\tau_b + \tau_p)k} \left[2\tau_p(\tau_b + \tau_p + kt)\mathcal{C}_1 + \tau_b(\tau_b + \tau_p + \tau_b k + kt)\mathcal{C}_2 - \tau_b(\tau_b + \tau_p + \tau_b k)\mathcal{C}_2 \cosh \frac{\sqrt{\tau_b + \tau_p}}{\tau_b \sqrt{\tau_p}} t + \frac{\tau_b \sqrt{\tau_p}(\tau_b + \tau_p + \tau_b k)(2\mathcal{C}_1 - \mathcal{C}_2)}{\sqrt{\tau_b + \tau_p}} \sinh \frac{\sqrt{\tau_b + \tau_p}}{\tau_b \sqrt{\tau_p}} t \right]. \quad (60)$$

Note that in the last step we have used Eq. (49) to obtain λ^* from x^* and x_b^* .

The solutions obtained by this optimization procedure given in Eqs. (58)-(60) still depend on two unknown parameters \mathcal{C}_1 and \mathcal{C}_2 . We remark that the long-time limit of Eqs. (58)-(60) reveals that these unknowns encode the initial jump of \dot{x} and the initial value of the Lagrange-multiplier: $\mathcal{C}_1 = \dot{x}(0^+)$, $\mathcal{C}_2 = \Lambda(0^+)$, which depend on all parameters $\{\lambda_f, t_f, \tau_b, \tau_p, \kappa_b, k\}$.

Usually, these unknowns must be determined by a secondary minimization. Concretely, by inserting x^* and x_b^* , the work (52) can be expressed as function of $\mathcal{C}_1, \mathcal{C}_2$. Then, minimizing $\langle W \rangle(\mathcal{C}_1, \mathcal{C}_2)$ with respect to \mathcal{C}_1 yields the optimal value of $\mathcal{C}_1(\mathcal{C}_2)$ as a function of \mathcal{C}_2 . Inserting this result, subsequently minimizing $\langle W \rangle(\mathcal{C}_2)$ with respect to \mathcal{C}_2 , yields the optimal \mathcal{C}_2 . For the Maxwell fluid, this involves very cumbersome and nested expressions. However, this secondary minimization can be entirely avoided by making use of the symmetry property (3), which we have proven on general grounds. Postulating time-reversal symmetry of x^* and λ^* , immediately leads to analytical expressions for $\mathcal{C}_{1,2}(\lambda_f, t_f, \tau_b, \tau_p, \kappa_b, k)$; resulting in closed-form solutions $\{x^*, x_b^*, \lambda^*\}$.

As a consistency check, we have verified that the solutions obtained via the secondary minimization (without postulating the symmetry) match the analytical expressions found via the symmetry.

We note that Ref. [55] discusses optimal transport protocols for a viscoelastic system in the underdamped regime.

Machine learning algorithm

We chose an architecture and training procedure similar to Ref. [48]. We used feed-forward fully connected Deep Neural Networks (DNN) that take a single scalar input, and return a single scalar output value, and have three hidden layers of 4,4,10 nodes, as illustrated in Fig. 5. The set θ of weights and biases of all nodes parameterizes the DNN. We apply a ReLU activation function to the input layer, and tanh activation function to all other layers. The series of time steps $t_i \in \{\Delta t, 2\Delta t, \dots, t_f - \Delta t\}$ with $\Delta t > 0$ and $0 < t_i < t_f$, is sequentially given as input to the DNN, which returns as

sequential output the protocol values $\lambda(t_i)$. The protocol values at the boundaries $\lambda(0) = \lambda_0$ and $\lambda(t_f) = \lambda_f$ are fixed by the boundary conditions. Thus, there is a direct mapping between θ and a protocol λ . The DNN is initialized by setting all its parameters θ to zero, so that it generates protocols that are zero for all time steps $t_i < t_f$ and abruptly jump to λ_f at t_f . The work corresponding to such protocol is $\langle W \rangle_0 = \lambda_f^2/2 (\gamma_0/\tau_0)$, and the asymmetry is $\langle A_x + A_\lambda \rangle_0 = \lambda_f^2/2 (\Delta t/t_f)$. The training by a Monte-Carlo algorithm is done as follows. At each training step $n > 0$, a copy of the DNN θ_{n-1} is generated, and all parameters of the copy are perturbed by a Gaussian noise with zero mean and variance $\sigma = 0.03$, leading to θ'_n . For the protocol generated by θ'_n , we then numerically compute (by solving the Langevin equation) the new tentative value of the objective ϕ_n , for which we choose either the average work ($\phi_n \equiv \langle W \rangle_n$) or asymmetry parameter ($\phi_n \equiv \langle A_x + A_\lambda \rangle_n$). If $\phi'_n < \phi_{n-1}$ the DNN is replaced by the perturbed copy ($\theta_n \leftarrow \theta'_n$), and $\phi_n = \phi'_n$. Otherwise the copy DNN is rejected, and $\phi_n = \phi_{n-1}$. Expressing times in units of τ_0 , and space in units of λ_f , de-dimensionalises the dynamical equations, allowing us to keep κ and τ_0 generic. We chose $t_f = \tau_0$, and a temporal discretization of $\Delta t/t_f = 10^{-3}$.

EXTENDED DATA

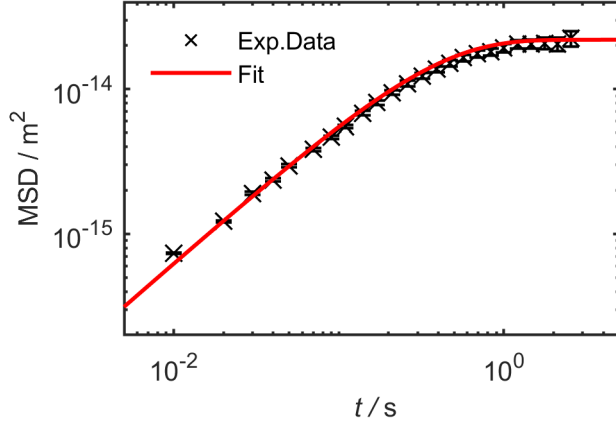


Fig. 6. Mean square displacement (MSD) of the $2.73\ \mu\text{m}$ particle in the viscous liquid. Symbols show the ensemble averaged data from experiments, errorbars correspond to the SEM. In full lines the analytical expression for the MSD of a colloid in a harmonic trap is plotted using the fitted parameters. The trap stiffness κ is fitted from the equilibrium distribution and the friction coefficient γ_0 is derived afterwards from the initial slop of the MSD [51].

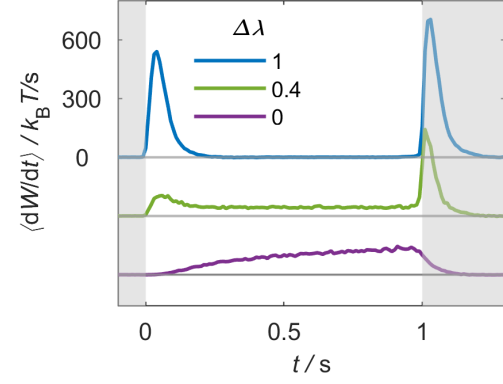


Fig. 7. Work traces in viscous fluid. Measured work increment $\langle dW/dt \rangle$ traces over time for selected protocols executed in a viscous fluid. Individual protocols are offset to negative values by $300\ k_B T$ for better readability, gray lines indicate the corresponding y-axis origin. The visible peaks result from jumps performed by λ . The work trace for the optimal protocol ($\Delta\lambda = 0.4\ \mu\text{m}$) shows a constant work increment during the protocol execution. This is in agreement with theoretical prediction, which give: $\langle dW/dt \rangle = m^2 \tau_0$, (with the slope m of the protocol and the trap relaxation time τ_0) for all $0 < t < t_f$